Aqueous Zinc Ion Storage in MoS$_2$ by Tuning the Intercalation Energy

Hanfeng Liang,[1,†] Zhen Cao,[2,†] Fangwang Ming,[1] Wenli Zhang,[1] Dalaver H. Anjum,[3] Yi Cui,[4] Luigi Cavallo,[2] Husam N. Alshareef[1,*]

[1]Materials Science and Engineering, Physical Science and Engineering Division, [2]KAUST Catalysis Center, [3]Imaging and Characterization Core Labs, King Abdullah University of Science and Technology (KAUST), Thuwal 23955-6900, Saudi Arabia.

[4]Department of Materials Science and Engineering, Stanford University, Stanford, California 94305, United States.

Abstract: Aqueous Zn-ion batteries present a low cost, safe, and high-energy battery technology, but suffer from the lack of suitable cathode materials because of the sluggish intercalation kinetics associated with the large size of hydrated zinc ions. Herein we report an effective and general strategy to transform inactive intercalation hosts into efficient Zn^{2+} storage materials through intercaltion energy tuning. Using MoS$_2$ as a model system, we show both experimentally and theoretically that even hosts with originally poor Zn^{2+} diffusivity can allow fast Zn^{2+} diffusion. Through simple interlayer spacing and hydrophilicity engineering that can be experimentally achieved by oxygen incorporation, the Zn^{2+} diffusivity is boosted by 3 orders of magnitude, effectively enabling the otherwise barely active MoS$_2$ to achieve a high capacity of 232 mAh g^{-1} that is 10 times as its pristine form. The strategy developed in our work can be generally applied for enhancing the ion

storage capacity of metal chalcogenides and other layered materials, making them promising cathodes for challenging multivalent ion batteries.

Keywords: MoS$_2$, oxygen incorporation, interlayer spacing tuning, hydrophilicity engineering, Zn^{2+} intercalation, zinc-ion battery

Lithium ion batteries (LIBs) have quickly dominated the power market of portable electronic devices since their first commercialization by SONY because of the high-energy density and long life span.[1-3] As the use of LIBs becomes widespread, concerns over their safety, access to easily mined Li, and the environmental impact have arisen.[4, 5] In this regard, aqueous rechargeable batteries (ARBs) based on earth abundant materials are promising alternatives.[6, 7] These batteries utilize water-based electrolytes, which are safe, low cost, and environmental friendly, but also possess much higher ionic conductivity (up to 1 S cm^{-1}) than that of the organic electrolytes (typically 1-10 mS cm^{-1}). Among various ARBs, aqueous Zn-ion batteries (ZIBs) have attracted increasing attention because of the distinctive merits of Zn metal anodes, such as low cost and high global production, high energy density (5851 mAh cm^{-3}), and relatively low electrode potential (-0.762 V vs SHE, or standard hydrogen electrode).[8-10] Compared with Li or Na, the bivalent Zn involves a two-electron transfer during charge/discharge and therefore enables a large storage capacity for the same number of ion insertion. On the other hand, though the ionic size of Zn (139 pm) is smaller than that of Li (182 pm) and Na (227 pm), its divalency causes strong interaction with water molecules and a Zn ion forms stable clathrate structure with a large size of 5.5 Å in aqueous solution (Figure 1a). Each Zn^{2+} can coordinate with 6 surrounding water molecules, resulting in additional difficulty in Zn^{2+} diffusion and intercalation. Commonly established intercalation hosts for Li and Na storage such as spinel,[11-13] layered oxides,[14-16] and chalcogenides[17-21] generally suffer from sluggish electrode kinetics in ZIBs and thus low capacity. Vanadium

oxides have recently shown promising Zn-ion storage properties,[22-25] but the dissolution of V in aqueous electrolytes remains a big challenge.[26] The Chevrel phase Mo_6S_8 is stable and has been studied as Zn^{2+} intercalation host for decades,[27, 28] yet a low Zn^{2+} storage capacity of 60 mA h g^{-1} at 0.06 A g^{-1} was achieved.[29] The high Zn^{2+} intercalation energy barrier is supposed to be responsible for the inferior performance.
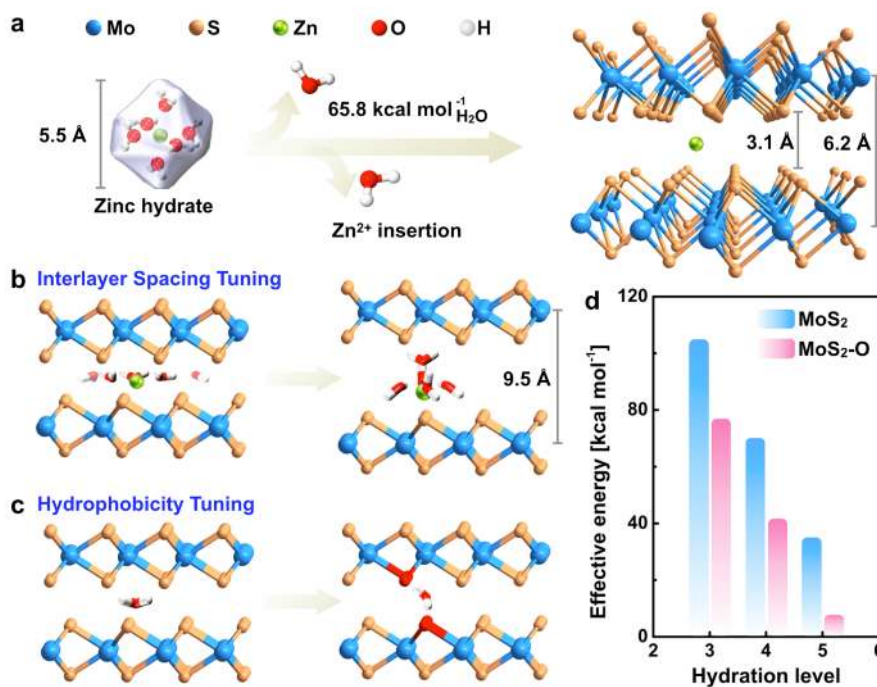

Figure 1. Schematic illustration of strategies developed in this work to enhance Zn^{2+} diffusion kinetics. (a) In pristine MoS_2, the interlayer spacing is limited and thus the intercalation of Zn hydrate is unlikely to proceed due to the huge energy barrier, resulting in the considerably low Zn^{2+} storage capacity. (b) Interlayer expanded MoS_2 has significantly lower Zn^{2+} intercalation energy because of the large scale of preservation of the Zn hydrate structure. (c) Hydrophilicity tuning strengthens the Zn^{II}-H_2O-O interaction and therefore promotes Zn^{2+} diffusion. (d) Theoretically calculated effective energy against the hydration level of Zn^{2+}.

In this work, we suggest a general and effective strategy to reduce the intercalation

energy barrier and therefore to increase the intrinsic Zn^{2+} diffusivity as well as to facilitate its intercalation into layered hosts. Using one of the most extensively studied Li/Na host materials, i.e. the layered chalcogenide MoS_2, as a model compound, we show that even hosts with originally poor Zn^{2+} diffusivity would allow fast Zn^{2+} diffusion through the interlayer spacing and hydrophilicity engineering, which can be experimentally achieved by oxygen incorporation. The Zn-intercalation chemistry was investigated by combined theoretical calculation and electrochemical analysis. Our result suggests that a small amount of oxygen incorporation (5%) into MoS_2 not only increases the interlayer spacing from 6.2 to 9.5 Å, but also improves the hydrophilicity and therefore significantly lowers the Zn^{2+} intercalation energy. As a result, improvements of three orders of magnitude in Zn^{2+} diffusivity and 10 times in Zn^{2+} storage capacity were observed.

We first performed density functional theory (DFT) calculations to evaluate the intercalation behavior of Zn^{2+} in MoS_2. In pristine MoS_2, the distance between the two intermediate MoS_2 layers (3.1 Å) is too small, therefore the intercalation of large Zn^{2+} hydrate (5.5 Å) is unlikely to proceed. The intercalation process however, should be accompanied with breaking of Zn^{II}-H_2O bonds. Our calculation result demonstrates a 66 kcal mol^{-1} energy input per coordination (Zn-O) bond. The optimized intercalated Zn^{2+} should replace all the Zn^{II}-OH_2 bonds by the Zn^{II}-S bonds (Figure 1a), leading to a large penalty and considerably sluggish Zn^{2+} diffusion. The energy requirement, however, can be decreased as long as the Zn^{2+} hydration structure is maintained at the largest scale. This can be achieved through the increment of the distance between the two intermediate MoS_2 layers. We note that alkaline ions (Li^+ and Na^+) can be readily intercalated into MoS_2, thus even slight interlayer spacing increments (e.g. 0.1-0.8 Å) of MoS_2 can lead to considerably enhanced performance.[30-32] However, given the huge size of Zn hydrate compared to Li^+ and Na^+, a significantly lager enlargement in interlayer spacing is needed to achieve comparable

performance. We have systematically investigated the correlation between the interlayer distance and the largest maintained Zn^{II}-H_2O bonds. With a 3 Å distance increment, the MoS_2 can incorporate Zn^{2+} cations with 5 water molecules as solvation shell, indicating only one Zn^{II}-H_2O needs to be broken during the intercalation process (Figure 1b) and therefore significantly less energy is required. On the other hand, the layered MoS_2 demonstrates a hydrophobic feature, indicating an unfavorable intercalation process due to the weak interaction between Zn^{II}-H_2O and S. Replacing the sulfur by oxygen atoms however, can modify the property of the MoS_2 layers, leading to an enhanced hydrophilicity and therefore stronger Zn^{II}-H_2O-O interaction (Figure 1c). In this way, the intercalation energy can be further lowered. Figure 1d visualizes the effective energy required against the hydrate level of Zn^{2+} cations. As the interlayer spacing of MoS_2 increases, the number of destroyed Zn^{II}-H_2O bonds is decreased and thus lower energy is achieved. For example, the energy input for the intercalation of Zn^{2+} with 5 water molecules is 34.8 kcal mol^{-1}, much lower than 104.5 kcal mol^{-1} for Zn^{2+} with 3 water molecules. This number is further greatly lowered to 7.8 kcal mol^{-1} for the oxygen incorporated MoS_2. These simulations strongly suggest that the interlayer spacing and hydrophilicity tuning can greatly facilitate the intercalation kinetics of Zn^{2+} cations in MoS_2 and generally, the large family of layered metal chalcogenides.

We then set out to synthesize MoS_2 nanosheets by hydrothermally reacting 64 mmol of $CS(NH_2)_2$ (thiourea) with 2.1 mmol of $(NH_4)_6Mo_7O_{24} \cdot 4H_2O$ (ammonium molybdate tetrahydrate) in water at 220 ℃ for 24 h (see Experimental details, Supporting Information).[33] At a lower reaction temperature, i.e. 180 ℃, the molybdate precursor might not completely decompose and the remaining Mo-O bonds can react with thiourea to form the oxygen incorporated MoS_2 (MoS_2-O).[33] The presence of O in MoS_2-O was confirmed by the X-ray photoelectron spectroscopy (XPS) analysis. The O 1s spectrum of MoS_2-O shows an additional peak at 530.6 eV compared with that of pristine MoS_2 (Figure S1, Supporting

Information), which can be assigned to the Mo-O bonds.[34] The water contact angle of the MoS$_2$ decreases from 127 to 110° after the oxygen incorporation (Figure S2, Supporting Information), suggesting an improved hydrophilicity. Interestingly, the MoS$_2$-O also has a large interlayer spacing of 9.5 Å. That is, both the interlayer spacing and hydrophilicity tuning can be achieved in one step by oxygen incorporation. The samples were then characterized by X-ray diffractometry (XRD). As shown in Figure 2a, the interlayer spacing of pristine MoS$_2$ is calculated to be 6.2 Å according to the Bragg's formula. For MoS$_2$-O, two new peaks with diploid relationship appear at 2θ angles of 9.3 and 18.6°, corresponding to the (002) and (004) reflections of layered MoS$_2$ with an interlayer spacing of 9.5 Å. We note that NH$_3$ and NH$_4^+$ ions can intercalate into some chalcogenides such as TiS$_2$[35] and MoS$_2$,[36] and consequently expand the interlayer spacings. However, the sharp diffraction peaks indicate that the expanded interlayer spacing is unlikely caused by NH$_3$/NH$_4^+$ intercalation. Further, the comparison of the Fourier-transform infrared (FTIR) spectra of MoS$_2$-O and the molybdate precursor (NH$_4$)$_6$Mo$_7$O$_{24}$•4H$_2$O confirms the absence of the adsorption peaks associated with the v_4(H–N–H) bending (1407 cm^{-1}) and v_3(N–H) asymmetric stretching (3050-3300 cm^{-1})[37-39] in MoS$_2$-O (Figure S3, Supporting Information). We further conducted the thermogravimetric analysis (TGA) and the result shows that there are two steps of weight loss (Figure S4a, Supporting Information). The 4.6% weight loss of MoS$_2$-O below 350 ℃ is due to the removal of loosely adsorbed water, whereas the 2.1% weight loss above 350 ℃ corresponds to the removal of tightly-bound water that most likely exists between the MoS$_2$-O layers. We further collected XRD pattern of the MoS$_2$-O after the TGA analysis (i.e. after the removal of both adsorbed and intercalated water) and found that the interlayer spacing reduces from 9.5 to 6.2 Å (Figure S4b, Supporting Information). In contrast, there is neglible weight loss (~0.4%) of MoS$_2$ above 350 ℃, that is, no trapped water. Further, the interlayer distance doesn't change after the TGA analysis. These results suggest that the interlayer

expansion of MoS_2-O is likely due to the water intercalation.

It is worth mentioning that MoS_2 is intrinsically hydrophobic, therefore the water intercalation is generally difficult even at high temperatures (e.g. 220 ℃). However, it seems the water intercalation can proceed at 180 ℃ in MoS_2-O sample. Though the origin is not clear, we believe that the oxygen incorporation plays a critical role (the presence of incorporated O was further confirmed by the EDS analysis of MoS_2-O after TGA, see Figure S5, Supporting Information). The smaller size of O atoms (48 pm vs 88 pm of S atoms) and the shorter Mo-O bonds (1.86 Å vs 2.42 Å for Mo-S bonds) weaken the van der Waals interactions between the two adjacent S layers, therefore leading to a slightly expanded interlayer spacing. Further, the oxygen incorporation improves the hydrophilicity. Both of them make the water intercalation in MoS_2-O sample possible. We used Ar plasma to etch O off MoS_2-O and found that the interlayer spacing of MoS_2-O decreases to 6.2 Å upon a 50 s-treatment (Figure S6, Supporting Information). This confirms the important role of oxygen incorporation in the interlayer space tuning of MoS_2. Raman analysis was further conducted to probe the property changes. As shown in Figure 2b, the frequency difference between A_1g and E_{2g}^1 of MoS_2-O gets 1.6 cm^{-1} smaller than that of MoS_2, suggesting a weakened interlayer interaction.[40, 41] Despite the difference in interlayer spacing, both the MoS_2 and MoS_2-O compose of dense and uniform nanosheet arrays (Figure 2c and Figure S7, Supporting Information), the typical morphology of layered materials. The elemental maps of MoS_2-O confirm the even distribution of Mo, S, and O (Figure 2d). Together with the XPS, this verifies the oxygen incorporation of MoS_2 rather than the surface oxidation. The ratio of O is determined to be 5% based on the electron dispersive spectroscopy (EDS) analysis, giving a stoichiometric formula of $MoS_{1.95}O_{0.05}$. The difference in interlayer spacing of MoS_2-O (Figure 2e) and MoS_2 (Figure 2f) was further confirmed by transmission electron microscopy (TEM) observation, which reveals interlayer distances of 9.5 and 6.2 Å

respectively, in agreement with the XRD result. Our calculation suggests that Zn^{2+} intercalation energy can be dramatically decreased through both the interlayer spacing and hydrophilicity tuning. The as-synthesized MoS_2-O provides a perfect platform to verify the efficacy of our strategy in enhancing the Zn^{2+} (or other multivalent ions with large intercalation barrier) storage capacity of layered intercalation hosts.
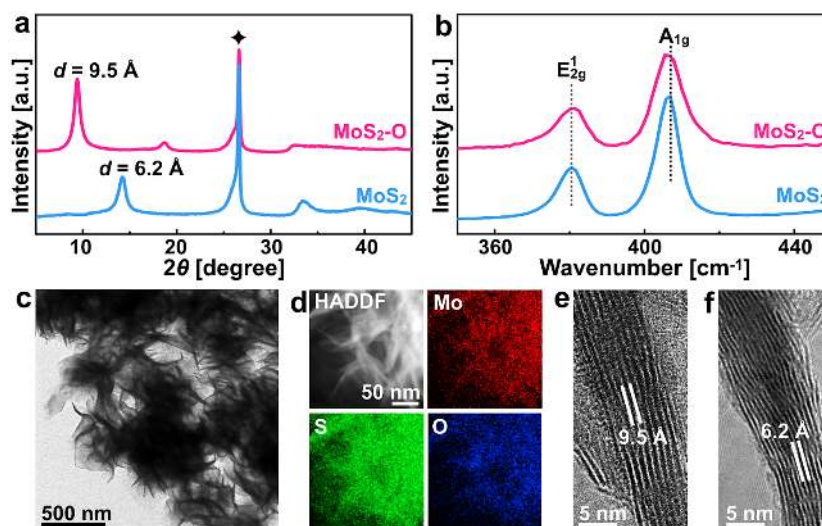

Figure 2. Structural characterization of MoS_2-O nanosheets. (a) XRD patterns and (b) Raman spectra of MoS_2-O and MoS_2 nanosheets. The asterisk in a presents the diffraction peak of carbon paper. (c) TEM image, (d) elemental maps, and (e) HRTEM image of MoS_2-O nanosheets. (f) HRTEM image of MoS_2 nanosheets.

The Zn^{2+} intercalation was investigated with CR2032-type coin cells comprising MoS_2-O (or MoS_2) cathode and Zn metal anode with a glass fiber separator in between, and a 3 M $Zn(CF_3SO_3)_2$ electrolyte. Figure 3a compares the cyclic voltammetry (CV) curves of the first three cycles of MoS_2-O and MoS_2 recorded at 0.1 mV s^{-1}. Both electrodes show an anodic peak at around 1.34 V vs Zn^{2+}/Zn that is associated with the oxidation of Mo^{4+} to Mo^{6+}. Notably, the MoS_2-O possesses an intense cathodic peak at 0.62 V that is related to the Zn^{2+} intercalation (it may cover or merge with the reduction peak of Mo^{6+}/Mo^{4+}), whereas the

anodic peak at 1.10 V corresponds to the Zn^{2+} deintercalation. In sharp contrast, the peaks of

Zn^{2+} intercalation/deintercalation are negligible in MoS_2 electrode (Figure S4, Supporting

Information), which indicates a much more sluggish Zn^{2+} intercalation kinetics. The 2nd and

3rd CV cycles are nearly overlapped for both electrodes, suggesting the good reversibility.

The charge-discharge (CD) profiles of MoS_2-O and MoS_2 are consistent with the CV result

(Figure 3b and Figure S8, Supporting Information), where an intercalation plateau at around

0.6 V is observed for MoS_2-O. The specific capacity of MoS_2 electrode at 0.1 A g^{-1} is merely

21 mAh g^{-1}. Interestingly, this number is close to that of Mg-ion battery with unmodified

MoS_2, where the intercalation of divalent Mg^{2+} is also very difficult.[40] The MoS_2-O electrode,

however, delivers a dramatically larger capacity of 232 mAh g^{-1}, significantly higher than

that reported for the well-known Zn^{2+} intercalation host, i.e. the Chevrel phase Mo_6S_8 (60 mA

h g^{-1} at 0.06 A g^{-1}),[29, 42] and more than 10 times as high as that of pristine MoS_2 (also see the

comparison in Table S1). The over 50% enlargement in interlayer spacing (9.5 vs 6.2 Å) may

not fully justify the huge boost in capacity, and we believe that the improved hydrophilicity

by oxygen incorporation is also critical. In fact, oxygen incorporation greatly lowers the

required energy input from 34.8 to 7.8 kcal mol^{-1} as suggested by our calculations. The

removal of oxygen by plasma results in dramatically smaller Zn^{2+} storage capacity (Figure S9,

Supporting Information). However, further oxygen incorporation (~8%) would lead to

stronger interactions of the MoS_2 host and Zn hydrate, which consequently results in

difficulty in Zn^{2+} extraction and therefore inferior performance (Figure S10, Supporting

Information). This result suggests that in order to achieve the optimal performance, the

interactions of MoS_2 host and the intercalated Zn hydrate should be neither too strong nor too

weak. Figure 3c compares the rate capability of the two electrodes. Both MoS_2-O and MoS_2

show stable cycling performance even at high rates. However, the MoS_2-O always delivers a

much higher capacity under different current densities. At the high current density of 1 A g^{-1},

43% of the capacity (98 mAh g^{-1}) obtained at 0.1 A g^{-1} was retained with MoS$_2$-O, compared to 31% capacity (7 mAh g^{-1}) retention of MoS$_2$ (Figure S11a, Supporting Information). The stability was further evaluated at a high current density of 1 A g^{-1}. A 68% capacity retention was achieved after 2000 cycles for MoS$_2$-O, compared with 61% retention for MoS$_2$, with the efficiency approaching 100% for both electrodes (Figure S11b, Supporting Information). After cycling, both materials maintain the overall sheet-like morphology though become more aggregated (Figure S12, Supporting Information).
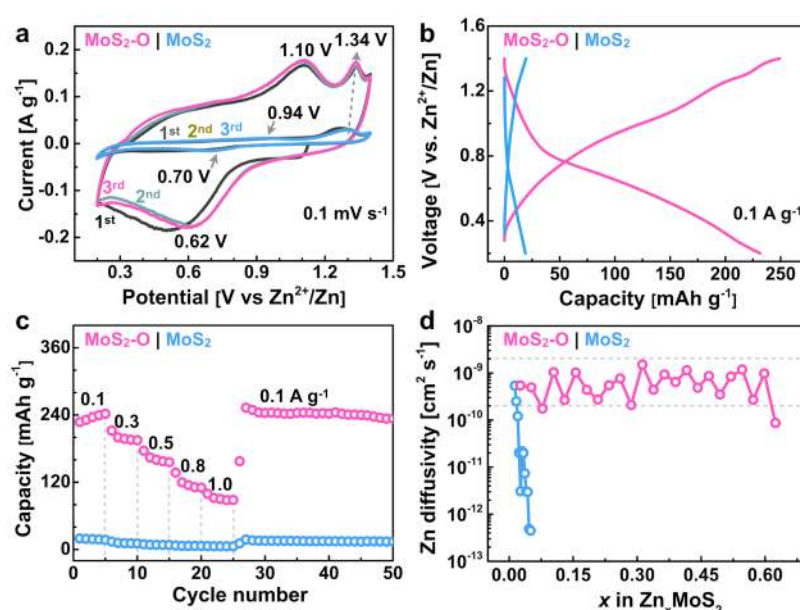

Figure 3. Electrochemical Zn-ion storage properties and kinetic analysis of the MoS$_2$-O and MoS$_2$. (a) CV curves of the first three cycles collected at a scan rate of 0.1 mV s^{-1}. (b) Discharge-charge profiles at 0.1 A g^{-1}. (c) Cycling stability at various current densities. (d) The Zn^{2+} diffusivity measured with GITT as a function of the concentration of intercalated Zn^{2+}. The x in Zn$_x$MoS$_2$ was calculated based on the discharge capacity.

To scrutinize the Zn^{2+} intercalation process of MoS$_2$-O and MoS$_2$, we studied the solid-state diffusion kinetics by galvanostatic intermittent titration technique (GITT), a method that has been widely applied to determine the ion diffusivity and thus to provide insight into the

electrode kinetics.[43] For MoS$_2$-O, the Zn^{2+} diffusivity is within 9×10^{-8}-10^{-9} cm^2 s^{-1} over the entire intercalation process (Figure 3d, see the raw GITT data in Figure S13, Supporting Information), suggesting the relatively facile kinetics. In contrast, the Zn^{2+} diffusivity in unmodified MoS$_2$ immediately hits the 10^{-11} cm^2 s^{-1} region as the Zn^{2+} intercalation begins, and quickly reaches an end at 8×10^{-12} cm^{-2} s^{-1}. The ion diffusion is so slow that further Zn^{2+} intercalation cannot proceed and hence the poor Zn^{2+} storage capacity. Only ~0.06 mol Zn^{2+} per MoS$_2$ is intercalated (note both the intercalation and surface redox reaction contribute to the capacity, therefore the real number should be even smaller), in sharp contrast to nearly 0.7 mol Zn^{2+} per MoS$_2$-O. This result experimentally confirms the effectiveness of our strategy to facilitate the Zn^{2+} intercalation in layered chalcogenide hosts through both interlayer spacing and hydrophilicity engineering, and is consistent with our theoretical simulation. The optimized MoS$_2$-O facilitates Zn^{2+} diffusivity and brings down the intercalation energy, and therefore achieves high capacity.

The different Zn^{2+} intercalation behaviors were further revealed by TEM observation. After the discharge process, the interlayer spacing of MoS$_2$ remains 6.2 Å, suggesting that Zn^{2+} barely intercalates into the host lattice (Figure 4a). Whereas it increases from 9.5 to 10.7 Å for MoS$_2$-O, again confirming the successful intercalation of Zn^{2+}. The elemental mapping further suggests that the Zn^{2+} ions are intercalated into MoS$_2$-O host (Figure S14, Supporting Information). Experimental and theoretical studies reveal that the intercalation of MoS$_2$ by alkali ions (e.g. Li$^+$) is accompanied by significant changes in both the electronic and crystallographic structure of the host lattice.[44] By analogy, we believe that the Zn^{2+} intercalation would also result in such changes. Indeed, HRTEM images reveal that the MoS$_2$-O after discharge consists of structurally distinct domains. Besides the common honeycomb lattice intensity variations in 2H MoS$_2$, a predominate fraction of trigonal intensity variations is observed (Figure 4b), suggesting the 1T polymorph in MoS$_2$-O after

Zn^{2+} intercalation.[45] This is further supported by Raman analysis (Figure 4c). Compared to the pristine MoS_2-O, the A_{1g} peak of the discharged one becomes broader and the relative intensity ratio of A_{1g}/E^1_{2g} decreases from 2.1 to 1.2 resulting from the intercalation of Zn^{2+}. Further, except for the peaks originating from the 2H MoS_2 (A_{1g}, E^1_{2g} and E_{1g} at 404, 377, and 285 cm^{-1}, respectively),[46] additional peaks at 147 (J1), 236 (J2), and 336 (J3) cm^{-1} arising from the 1T phase[47] emerge, in agreement with our TEM observation. The 2H to 1T phase transition increases the conductivity as well as improves the hydrophilicity[48] and should be responsible for the capacity increase in the initial cycles (Figure 3c). In contrast, the Raman spectrum of pristine MoS_2 doesn't show significant changes after the discharge process. It should be pointed out that MoS_2 with an interlayer spacing of 7.0 Å has previously been used for aqueous zinc ion battery, however, no phase transformation of MoS_2 was observed during the discharge process.[49] This indicates that a large interlayer spacing is essential for the Zn^{2+} intercalation of MoS_2 and consequently the 2H to 1T phase transformation. We note that 1T MoS_2 has found many promising applications[48, 50, 51] due to its metallic nature, and it is typically produced by Li^+ intercalation of semiconducting 2H MoS_2 with *n*-butyllithium for more than a day.[51-53] While this approach is effective, the exothermic reaction of water with Li^+ intercalated MoS_2 (Li_xMoS_2) raises safety issues.[52-54] The Zn^{2+} intercalation of 2H MoS_2 demonstrated in this work however, promises an effective and safer way to produce 1T MoS_2 in aqueous solution.
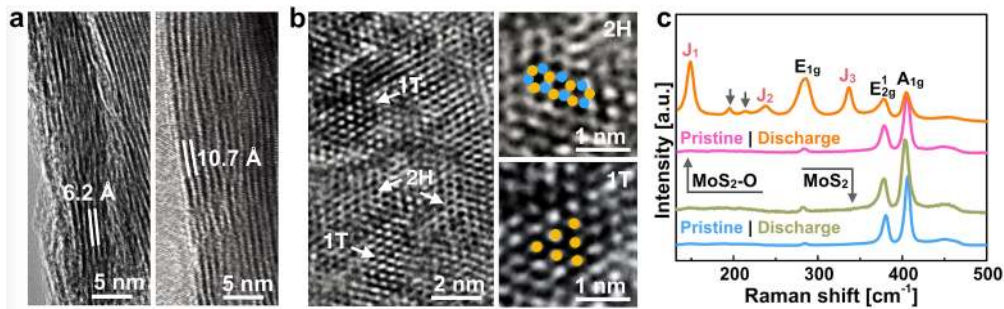

Figure 4. Structural characterization of MoS_2-O and MoS_2 after the discharge process (at 100

mA g^{-1}). (a) TEM images of MoS$_2$ (left) and MoS$_2$-O. (b) HRTEM images of MoS$_2$-O. (c) Comparison of the Raman spectra.

The interlayers of Zn^{2+} intercalated MoS$_2$-O are expanded but not exfoliated or damaged, possibly because of the strong contact with the carbon paper substrate. Intriguingly, the structural changes are reversible during the charge/discharge process. This was first verified by SEM observation. The MoS$_2$-O nanosheets were thickened upon discharging (Zn^{2+} intercalation), but became gradually thinner during charge (Figure S15, Supporting Information). Besides this, we also observed that additional nanorods are produced and accumulated during discharge process, but then dissolved upon charging. This interesting phenomenon drove us to further study the reaction mechanism involved in the Zn-ion battery with MoS$_2$-O. We performed XRD and XPS study on the MoS$_2$-O electrodes collected at different charge-discharge voltages (Figure 5a). The *ex situ* XRD patterns are shown in Figure 5b. As intercalation proceeds (upon discharging), the (002) diffraction peak becomes broader, indicating an occurrence of a stacking fault along the *c*-axis resulted from cation intercalation.[37] The new peak positions arising from Zn^{2+} (de)intercalation are indicated as peaks (001)* and (002)* to differentiate them from those obtained in pristine electrode. We note that the (001)* peak gradually shifts to lower angles, which is an indication of interlayer expansion. The interlayer spacing increases to 10.7 Å (corresponding to a 2θ degree of 8.3°) when the electrode reaches 0.2 V (status D), consistent with the TEM observation (Figure 4a). As we discussed earlier, the intercalation process would result not only in structural but also electronic changes that induce the phase transition of 2H to 1T MoS$_2$. Evidently, a new diffraction peak indicated as (002)* emerges. Note that both 2H and 1T MoS$_2$ show such characteristic peak. Together with the Raman (Figure 4c) and XPS (as will be discussed later) results however, we believe that the 2H to 1T phase transition occurs upon discharging. Upon

charging, the (001)* peak shifts back to a 2θ angle of 9.0°, corresponding to an interlayer spacing of 9.8 Å, slightly larger than the original 9.5 Å. This result agrees with the SEM observation, where the nanosheets of the fully charged electrode are still slightly thicker than the pristine sample (Figure S15, Supporting Information). We also noted that when the electrode reaches 0.2 V, a new phase with sharp and intense diffraction peak that distinctly differs from those of MoS_2 is observed. This new peak is likely attributed to the $Zn_4(OH)_6SO_4 \cdot 5H_2O$ (ZHS), which was precipitated from the electrolyte. This explains the nanorods in the discharged MoS_2-O electrode (Figure S15, Supporting Information). Interestingly, the precipitate could undergo dissolution upon charging, indicated by the disappearance of the intense diffraction peak when the electrode is charged to 1.4 V, consistent with our SEM observation. This phenomenon has already been observed in various cathode materials such as $Mg_xV_2O_5$[22] and $Na_2V_6O_{16}$[55] in $ZnSO_4$ electrolyte and is supposed to be related to the pH evolution of the electrolyte during battery operation.[56] However, it rarely occurs in $Zn(CF_3SO_3)_2$ electrolyte. Interestingly, when the MoS_2 was used as the cathode, no ZHS was formed as confirmed by the XRD and SEM result (Figure S16, Supporting Information). Though the reason is not clear, we suspect that the MoS_2-O might catalyze the formation of the ZHS due to the high electrocatalytic activity. The formation of ZHS would consume OH^- and therefore promote the water dissociation to produces H^+, which might then intercalate into the cathodes (e.g. $NaV_3O_8 \cdot 1.5H_2O$) along with Zn^{2+}.[26] The H^+ intercalation might also proceed in MoS_2-O but the contribution to the overall capacity is supposed to be low (see additional data in Figure S17, Supporting Information and detailed analysis). The XPS analysis provides further proof of the formation of ZHS. The discharged electrode shows two Zn species (Zn $2p_{3/2}$ at 1021 and 1023 eV) that correspond to the sulfate precipitate and intercalated Zn^{2+} respectively, which are absent before the reaction (Figure 5c). The former peak vanishes in the charge process, confirming the reversible

precipitation/dissolution of the zinc hydroxide sulfate. Whereas the peak associated with intercalated Zn^{2+} is still apparent but with significantly reduced intensity, suggesting that a small amount of Zn^{2+} (~1.5% based on the EDS analysis, see Figure S15 in Supporting Information) cannot be deintercalated, possibly due to the applied voltage and/or the relatively strong interactions between Zn hydrate and MoS_2-O. The uniform distribution of Zn in MoS_2-O (Figure S18, Supporting Information) indicates that the residual Zn does not come from the precipitate but the intercalated Zn^{2+}. This conclusion agrees well with the XRD and SEM results. The Zn 2p XPS spectra clearly reveal a Zn^{2+} intercalation/deintercalation process, which inevitably causes the structural and electronic changes of MoS_2-O. The Mo 3d XPS spectrum of the pristine electrode suggests two distinct species of 2H MoS_2 and MoS_xO_y, along with a small amount of Mo^{6+} resulting from surface oxidation.[57] After the electrode was discharged to 0.2 V, the S 2s peak shifted by ~0.8 eV to a lower binding energy. In addition, the peak fitting of the Mo 3d spectrum also indicates a new component has emerged with peaks located at binding energies that are ~0.8 eV lower than those of 2H MoS_2, which can be assigned to the 1T phase.[58] This result further validates the findings from TEM and Raman analyses (Figure 4) that 1T MoS_2 is produced by Zn^{2+} intercalation. Deconvolution of the Mo 3d region reveals a 1T phase concentration of 78% (against 22% for 2H phase). Because the 1T MoS_2 is metastable, the surface is easily oxidized upon air exposure. Consequently, a dramatic increase in peak intensity of Mo^{6+} species was observed. After recharging to 1.4 V, the electrode surface is dominated by Mo^{6+} species, because of the anodic oxidation starts at 1.34 V (see CVs in Figure 3a). Notably, the S 2s peak shifts back by ~0.8 eV, revealing a similar environment to that of the pristine electrode. Together with the absence of 1T component, this confirms the 1T to 2H MoS_2 phase transition upon Zn^{2+} deintercalation. Overall, the electrochemical reaction mechanism of the present MoS_2-O electrode with Zn can be explained on the basis of Zn^{2+}

intercalation/deintercalation into/from the layered host accompanied by the reversible 2H to 1T MoS_2 phase transition, in addition to the precipitation/dissolution of zinc hydroxide sulfate. It is worth mentioning that, however, the surface Mo^{4+}/Mo^{6+} redox reaction also contributes to the storage capacity. Both the intercalation and surface redox reactions are reversible as supported by the structural characterization results as well as the well-overlapped CV curves (Figure 3a).
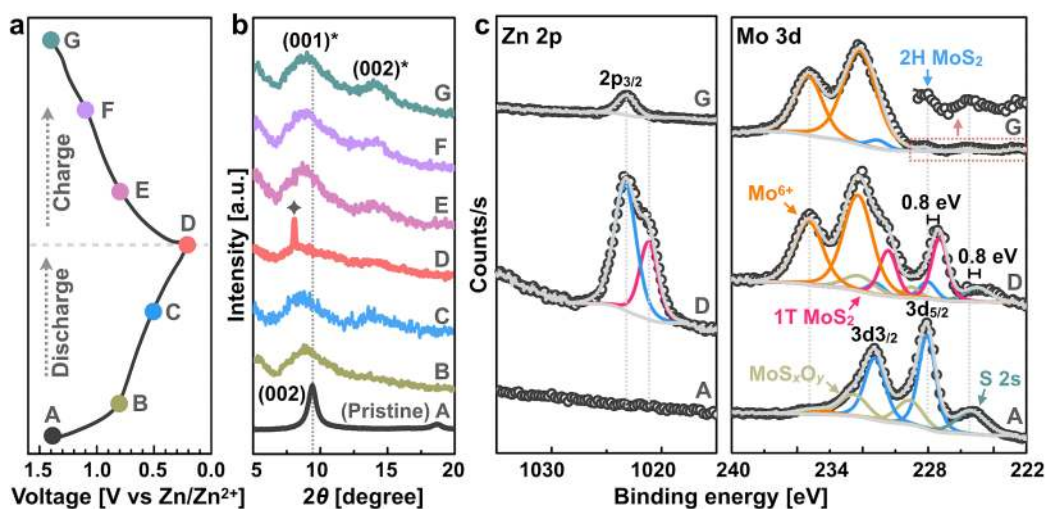

Figure 5. *Ex situ* study of the MoS_2-O electrodes. (a) Charge-discharge profile at 100 mA g^{-1}. (b) XRD patterns and (c) Zn 2p and Mo 3d XPS spectra at different charge/discharge voltages as indicated in a. The new diffraction peaks after intercalation in b are indicated as (001)* and (002)* to differentiate them from those obtained in pristine material.

In summary, we present a general and effective strategy by tuning both the interlayer spacing and hydrophilicity, and thus the intercalation energy to transform intrinsically inactive intercalation hosts into efficient Zn^{2+} storage materials. Using one of the most extensively studied Li/Na host materials, i.e. the layered chalcogenide MoS_2, as a model compound, we show both computationally and experimentally that the interlayer spacing and hydrophilicity tuning, which are achieved by oxygen incorporation, effectively boost the Zn^{2+} diffusion kinetics by three orders of magnitude. As a result, the capacity of the almost inactive MoS_2 increases by 10 times, and reaches 232 mAh g^{-1} at 100 mA g^{-1} that is

dramatically higher than the Chevrel phase chalcogenide Mo_6S_8 as well as many other intercalation host materials. The promoted Zn^{2+} intercalation in aqueous solution also promises an efficient and safe way to produce the metallic 1T MoS_2, which has found various promising applications but suffers from the safety issue in its preparation by the common Li^+ intercalation method. The approach of intercalation energy tuning developed in this work can be generally extended to enhance the ion storage performance of a large family of layered intercalation hosts, which creates new opportunities for the development of advanced materials for next-generation energy storage.

ASSOCIATED CONTENT

Supporting Information. The following files are available free of charge.

Experimental details and additional supporting data as noted in the main text (PDF).

AUTHOR INFORMATION

Corresponding Author

*E-mail: husam.alshareef@kaust.edu.sa

Notes

[†]These authors contributed equally. The authors declare no competing financial interest.

ACKNOWLEDGMENT

supercomputers.

REFERENCES

(1)   Lu, L.; Han, X.; Li, J.; Hua, J.; Ouyang, M. *J. Power Sources* **2013**, *226*, 272-288.

(2)   Etacheri, V.; Marom, R.; Elazari, R.; Salitra, G.; Aurbach, D. *Energy Environ. Sci.* **2011**, *4*, 3243-3262.

(3)   Dunn, B.; Kamath, H.; Tarascon, J.-M. *Science* **2011**, *334*, 928-935.

(4)   Jacoby, M. *Chem. Eng. News* **2013**, *91*, 33-37.

(5)   Wanger, T. C. *Conserv. Lett.* **2011**, *4*, 202-206.

(6)   Kim, H.; Hong, J.; Park, K.-Y.; Kim, H.; Kim, S.-W.; Kang, K. *Chem. Rev.* **2014**, *114*, 11788-11827.

(7)   Liu, J.; Xu, C.; Chen, Z.; Ni, S.; Shen, Z. X. *Green Energy Environ.* **2018**, *3*, 20-41.

(8)   Ming, J.; Guo, J.; Xia, C.; Wang, W.; Alshareef, H. N. *Mater. Sci. Eng. R* **2019**, *135*, 58-84.

(9)   Konarov, A.; Voronina, N.; Jo, J. H.; Bakenov, Z.; Sun, Y.-K.; Myung, S.-T. *ACS Energy Lett.* **2018**, *3*, 2620-2640.

(10)   Song, M.; Tan, H.; Chao, D.; Fan, H. J. *Adv. Funct. Mater.* **2018**, *28*, 1802564.

(11)   Kim, D. K.; Muralidharan, P.; Lee, H.-W.; Ruffo, R.; Yang, Y.; Chan, C. K.; Peng, H.; Huggins, R. A.; Cui, Y. *Nano Lett.* **2008**, *8*, 3948-3952.

(12)   Hosono, E.; Kudo, T.; Honma, I.; Matsuda, H.; Zhou, H. *Nano Lett.* **2009**, *9*, 1045-1051.

(13)   Wang, Y.-Q.; Gu, L.; Guo, Y.-G.; Li, H.; He, X.-Q.; Tsukimoto, S.; Ikuhara, Y.; Wan, L.-J. *J. Am. Chem. Soc.* **2012**, *134*, 7874-7879.

(14)   Wang, Y.; Yu, X.; Xu, S.; Bai, J.; Xiao, R.; Hu, Y.-S.; Li, H.; Yang, X.-Q.; Chen, L.; Huang, X. *Nat. Commun.* **2013**, *4*, 2365.

(15)   Ohzuku, T.; Makimura, Y. *Chem. Lett.* **2001**, *30*, 744-745.

(16)   Chao, D.; Xia, X.; Liu, J.; Fan, Z.; Ng, C. F.; Lin, J.; Zhang, H.; Shen, Z. X.; Fan, H. J. *Adv. Mater.* **2014**, *26*, 5794-5800.

(17)   Qu, B.; Ma, C.; Ji, G.; Xu, C.; Xu, J.; Meng, Y. S.; Wang, T.; Lee, J. Y. *Adv. Mater.* **2014**, *26*, 3854-3859.

(18)   Zhang, F.; Xia, C.; Zhu, J.; Ahmed, B.; Liang, H.; Velusamy, D. B.; Schwingenschlögl, U.; Alshareef, H. N. *Adv. Energy Mater.* **2016**, *6*, 1601188.

(19)   Ahmed, B.; Anjum, D. H.; Hedhili, M. N.; Alshareef, H. N. *Small* **2015**, *11*, 4341-4350.

(20)   Chao, D.; Zhu, C.; Yang, P.; Xia, X.; Liu, J.; Wang, J.; Fan, X.; Savilov, S. V.; Lin, J.; Fan, H. J. *Nat. Commun.* **2016**, *7*, 12122.

(21)   Chao, D.; Ouyang, B.; Liang, P.; Huong, T. T. T.; Jia, G.; Huang, H.; Xia, X.; Rawat, R. S.; Fan, H. J. *Adv. Mater.* **2018**, *30*, 1804833.

(22)   Ming, F.; Liang, H.; Lei, Y.; Kandambeth, S.; Eddaoudi, M.; Alshareef, H. N. *ACS Energy Lett.* **2018**, *3*, 2602-2609.

(23)   Kundu, D.; Adams, B. D.; Duffort, V.; Vajargah, S. H.; Nazar, L. F. *Nature Energy* **2016**, *1*, 16119.

(24)   Xia, C.; Guo, J.; Lei, Y.; Liang, H.; Zhao, C.; Alshareef, H. N. *Adv. Mater.* **2018**, *30*, 1705580.

(25)   Chao, D.; Zhu, C.; Song, M.; Liang, P.; Zhang, X.; Tiep, N. H.; Zhao, H.; Wang, J.; Wang, R.; Zhang, H. *Adv. Mater.* **2018**, *30*, 1803181.

(26)   Wan, F.; Zhang, L.; Dai, X.; Wang, X.; Niu, Z.; Chen, J. *Nat. Commun.* **2018**, *9*, 1656.

(27)   Gocke, E.; Schramm, W.; Dolscheid, P.; SchoE̲llhorn, R. *J. Solid State Chem.* **1987**, *70*, 71-81.

(28)   Schöllhorn, R.; Kümpers, M.; Besenhard, J. *Mater. Res. Bull.* **1977**, *12*, 781-788.

(29)   Cheng, Y.; Luo, L.; Zhong, L.; Chen, J.; Li, B.; Wang, W.; Mao, S. X.; Wang, C.; Sprenkle, V. L.; Li, G. *ACS Appl. Mater. Interfaces* **2016**, *8*, 13673-13677.

(30)   Hwang, H.; Kim, H.; Cho, J. *Nano Lett.* **2011**, *11*, 4826-4830.

(31)   Hu, Z.; Wang, L.; Zhang, K.; Wang, J.; Cheng, F.; Tao, Z.; Chen, J. *Angew. Chem. Int. Ed.* **2014**, *53*, 12794-12798.

(32)   Liu, H.; Su, D.; Zhou, R.; Sun, B.; Wang, G.; Qiao, S. Z. *Adv. Energy Mater.* **2012**, *2*, 970-975.

(33)   Xie, J.; Zhang, J.; Li, S.; Grote, F.; Zhang, X.; Zhang, H.; Wang, R.; Lei, Y.; Pan, B.; Xie, Y. *J. Am. Chem. Soc.* **2013**, *135*, 17881-17888.

(34)   Sun, Y.; Hu, X.; Luo, W.; Huang, Y. *ACS Nano* **2011**, *5*, 7100-7107.

(35)   Ong, E. W.; Eckert, J.; Dotson, L. A.; Glaunsinger, W. S. *Chem. Mater.* **1994**, *6*, 1946-1954.

(36)   Anto Jeffery, A.; Nethravathi, C.; Rajamathi, M. *J. Phys. Chem. C* **2014**, *118*, 1386-1396.

(37)   Esparcia, E. A.; Chae, M. S.; Ocon, J. D.; Hong, S.-T. *Chem. Mater.* **2018**.

(38)   Waddington, T. *J. Chem. Soc. (Resumed)* **1958**, 4340-4344.

(39)   Nyquist, R. A.; Kagel, R. O., *Handbook of infrared and raman spectra of inorganic compounds and organic salts: infrared spectra of inorganic compounds*. Academic press: San Diego, **1971**.

(40)   Liang, Y.; Yoo, H. D.; Li, Y.; Shuai, J.; Calderon, H. A.; Robles Hernandez, F. C.; Grabow, L. C.; Yao, Y. *Nano Lett.* **2015**, *15*, 2194-2202.

(41)   Lee, C.; Yan, H.; Brus, L. E.; Heinz, T. F.; Hone, J.; Ryu, S. *ACS Nano* **2010**, *4*, 2695-2700.

(42)   Chae, M. S.; Heo, J. W.; Lim, S.-C.; Hong, S.-T. *Inorg. Chem.* **2016**, *55*, 3294-3301.

(43)   Weppner, W.; Huggins, R. A. *J. Electrochem. Soc.* **1977**, *124*, 1569-1578.

(44)   Wang, H.; Lu, Z.; Xu, S.; Kong, D.; Cha, J. J.; Zheng, G.; Hsu, P.-C.; Yan, K.; Bradshaw, D.; Prinz, F. B. *Proc. Natl. Acad. Sci. U.S.A.* **2013**, *110*, 19701-19706.

(45)   Eda, G.; Fujita, T.; Yamaguchi, H.; Voiry, D.; Chen, M.; Chhowalla, M. *ACS Nano* **2012**, *6*, 7311-7317.

(46)   Li, H.; Zhang, Q.; Yap, C. C. R.; Tay, B. K.; Edwin, T. H. T.; Olivier, A.; Baillargeat, D. *Adv. Funct. Mater.* **2012**, *22*, 1385-1390.

(47)   Gupta, U.; Naidu, B.; Maitra, U.; Singh, A.; Shirodkar, S. N.; Waghmare, U. V.; Rao, C. *APL Materials* **2014**, *2*, 092802.

(48)   Acerce, M.; Voiry, D.; Chhowalla, M. *Nat. Nanotechnol.* **2015**, *10*, 313-318.

(49)   Li, H.; Yang, Q.; Mo, F.; Liang, G.; Liu, Z.; Tang, Z.; Ma, L.; Liu, J.; Shi, Z.; Zhi, C. *Energy Storage Mater.* **2018**, doi: 10.1016/j.ensm.2018.10.005.

(50)   Geng, X.; Jiao, Y.; Han, Y.; Mukhopadhyay, A.; Yang, L.; Zhu, H. *Adv. Funct. Mater.* **2017**, *27*, 1702998.

(51)   Lukowski, M. A.; Daniel, A. S.; Meng, F.; Forticaux, A.; Li, L.; Jin, S. *J. Am. Chem. Soc.* **2013**, *135*, 10274-10277.

(52)   Wang, Q. H.; Kalantar-Zadeh, K.; Kis, A.; Coleman, J. N.; Strano, M. S. *Nat. Nanotechnol.* **2012**, *7*, 699.

(53)   Eda, G.; Yamaguchi, H.; Voiry, D.; Fujita, T.; Chen, M.; Chhowalla, M. *Nano Lett.* **2011**, *11*, 5111-5116.

(54)   Joensen, P.; Frindt, R.; Morrison, S. R. *Mater. Res. Bull.* **1986**, *21*, 457-461.

(55)   Soundharrajan, V.; Sambandam, B.; Kim, S.; Alfaruqi, M. H.; Putro, D. Y.; Jo, J.; Kim, S.; Mathew, V.; Sun, Y.-K.; Kim, J. *Nano Lett.* **2018**, *18*, 2402-2410.

(56)   Lee, B.; Seo, H. R.; Lee, H. R.; Yoon, C. S.; Kim, J. H.; Chung, K. Y.; Cho, B. W.; Oh, S. H. *ChemSusChem* **2016**, *9*, 2948-2956.

(57)   Brown, N. M.; Cui, N.; McKinley, A. *Appl. Surf. Sci.* **1998**, *134*, 11-21.

(58)   Papageorgopoulos, C.; Jaegermann, W. *Surf. Sci.* **1995**, *338*, 83-93.

ToC